Air-stable metal hydride-polymer composites of $Mg(NH_2)_2$-LiH and TPX™

Hujun Cao,[a]* Prokopios Georgopanos,[b]* Giovanni Capurso,[a] Claudio Pistidda,[a] Fynn Weigelt,[b] Anna-Lisa Chaudhary,[a] Volkan Filiz,[b] Jo-Chi Tseng,[c] Michael T. Wharmby,[c] Martin Dornheim[a] Volker Abetz,[b, d] and Thomas Klassen[a,e]

a. Institute of Materials Research, Materials Technology, Helmholtz-Zentrum Geesthacht GmbH, Max-Planck-Straße 1, 21502, Geesthacht, Germany.

E-Mail: hujun.cao@hzg.de; Fax: + 49 4152 / 87-2625; Tel: +49 4152 / 87-2643

b. Institute of Polymer Research, Helmholtz-Zentrum Geesthacht GmbH, Max-Planck-Straße 1, 21502, Geesthacht, Germany.

E-Mail: prokopios.georgopanos@hzg.de; Fax: + 49 4152 / 87-2466; Tel: +49 4152 / 87-2420

c. Deutsches Elektronen-Synchrotron (DESY), Notkestraße 85, 22607 Hamburg, Germany.

d. Institute of Physical Chemistry, University of Hamburg, Martin-Luther-King-Platz 6, 20146 Hamburg, Germany.

e. Institute of Materials Technology, Helmut Schmidt University, Holstenhofweg 85, 22043 Hamburg, Germany.

Abstract

Light metal hydrides are prone to react with oxygen and/or water to produce oxides and/or hydroxides leading to reduction of hydrogen capacities, and deterioration of the hydrogen storage properties. It is therefore critical to address these issues when the materials are to be exposed to air or moisture. In this work, the combination of light metal hydrides, $Mg(NH_2)_2$-nLiH with polymethylpentene (TPX™), an air/moisture protective barrier is presented. It was found that the fabricated composites exhibit significant improvement of the metal hydrides stability in air. No oxidation reactions in air can be proven even after air exposure for 90 minutes. Extending the air-exposure time to 12 hours, the reversible hydrogen capacities of these composites are much higher and more stable than they are in the case of the pure metal hydrides. In comparison to the pure metal hydrides, the composites retain the same hydrogen loading capacities and kinetic properties, with respect to the metal hydrides contents. Further, *in situ* synchrotron radiation powder X-ray radiation diffraction (SR-PXRD) experiments reveal that the thermal decomposition reaction pathways of the 90 minutes air-exposed composites are the same under air or H_2 atmosphere. Moreover, morphology analysis confirms that the metal hydrides remain stable in the polymeric matrix and the three-dimensional integrity is retained, even after performing tens of de/re-hydrogenation cycles. The present study shows a promising way to fabricate air-stable metal hydride-polymer composite hydrogen storage materials that can be handled in ambient conditions.

Keywords: reactive hydride composite, air-stability, hydrogen storage, polymethylpentene

Introduction

The preparation of composite materials has been known for centuries with a variety of applications in everyday life.[1] Many composite materials derive from the combination of polymers, which usually have the role of the matrix, and filler materials such as, *e.g.*, fibers, ceramics or metal oxides, etc..[2, 3] The combination of such materials leads to new materials usually with more advanced properties or even better performance for specific applications such as in membranes[4, 5] or in energy applications.[6] Polymethylpentene under the trademark TPX™-RT18 of Mitsui Chemicals, INC., shortened to TPX hereafter, is a 4-methyl-1-pentene based polyolefin, similar to traditional polyolefin, with excellent gas permeability, heat and chemical resistance and strong hydrolysis resistance. Recently, polyolefines have been employed as matrices for composite materials due to their distinctive molecular structures, which display unique combinations of physical properties and characteristics.[7-9] The use of TPX as a matrix material for composite films is known in applications for gas separation, *e.g.*, in TPX/Al_2O_3 mixed-matrix membranes for CO_2/CH_4 separation. Nevertheless, until now, to the best of our knowledge, there are no references for the use of TPX polymers in composites used for hydrogen storage materials.

Composite materials have also received much attention in the hydrogen storage area recently, such as the approach of tailoring the thermodynamic properties by mixing two or more hydrogen-containing materials, denoted as Reactive Hydride Composites (RHC).[10-16] Amide-hydride composites are an example of such an approach. Such composites have been extensively investigated for hydrogen storage since 2002,[17-23][24] due to their advanced properties, such as thermodynamic stability, reversibility and high hydrogen capacity. $Mg(NH_2)_2$-xLiH, (x=2, 8/3, 4) systems were developed by different research groups in 2004.[25-28] The system where x = 2, namely, $Mg(NH_2)_2$-2LiH (hereafter labeled LMNH), has been considered as one of the most promising materials for on-board applications,[25] because of its suitable gravimetric hydrogen capacity (ca. 5.6 wt%) and dehydrogenation enthalpy (ΔH ca. 40 kJ (mol-H_2)$^{-1}$).[29] A lot of studies[30-41] were devoted to optimizing the hydrogen storage properties of $Mg(NH_2)_2$-2LiH, and these studies have shown that the best kinetic additives are KH and RbH. KH doped $Mg(NH_2)_2$-2LiH can reduce the peak temperature from ca. 190 °C to 130 °C. While its equilibrium H_2 pressure is roughly 2 bar at 107 °C.[42-45] In order to improve the reaction kinetics of $Mg(NH_2)_2$-2LiH composite even further, there is the need to modify the thermodynamics, allowing to release 1 bar H_2 in equilibrium conditions at much lower temperatures. Following this target, the thermodynamically optimized system $6Mg(NH_2)_2$-9LiH-$LiBH_4$ (hereafter labeled LMBNH) has been obtained by stabilizing the dehydrogenated product $LiNH_2$, which allows to release 1 bar H_2 at the equilibrium temperature of 64 °C.[46] In addition, $6Mg(NH_2)_2$-9LiH-$LiBH_4$ shows an excellent reversibility, its complete absorption time is less than 10 min and full absorption can be achieved at 90 °C after adding YCl_3 and Li_3N.[47] One drawback in the use of these amide-hydride systems is that after some de/re-hydrogenation cycles these systems lose their hydrogen storage capacities and reaction kinetics are reduced. One explanation for these changes is that amides and hydrides are prone to react with oxygen and/or water to produce oxides or hydroxides, thus contaminating the system. Another reason is that, during the de/re-hydrogenation cycles, the hydride microstructure coarsens, and the reactants phase separate over longer distances, increasing diffusion pathway lengths, thus slowing kinetics.[48] To overcome these drawbacks and reduce operating and manufacturing costs of the material systems, the production of air-stable hydrides would be a tremendous advantage. To date, only a few publications have been devoted to the investigation of the stability of amide-hydride composites in the presence of O_2, H_2O or air.[49, 50]

This work aims to solve this problem by deploying novel hydride-polymer composites. As already mentioned, the combination of metal hydride and polymer for hydrogen storage has not been addressed except for a few studies relating to poly(methyl methacrylate) - magnesium hydride composites for hydrogen storage[51-53] or acrylonitrile-butadiene-styrene copolymer (ABS)-$LaNi_5$ type metal hydride,[54] MnO anchored to poly(ether-ether-keton),[55] or ammonia borane in polystyrene.[56] Another energy storage application with a similar composite is the use of poly(acrylonitrile) in lithium batteries.[57] In this study, TPX has been selected as the host polymer, with the intention of protecting the metal hydrides from oxygen and water, whilst allowing the hydrogen to permeate through in order to enable hydrogen absorption or desorption. LMBNH and LMNH have been chosen as the active ingredients due to their low operating temperatures below 250 °C. Incorporating these materials into the TPX matrix (see Figure 1), the amide-hydride composites are enclosed in the polymer thus protecting the hydrides from O_2 and H_2O and contamination, leading to an almost air-stable hydrogen storage material. Additionally, owing to the confinement of hydrides within the TPX matrix, the amide-hydride composites remain in a stable position and do not coarsen to larger clusters and long-range phase separation is prevented. Detailed characterization regarding the hydrogen storage performance, the reaction mechanism as well as the air-stability and morphology are presented further on.

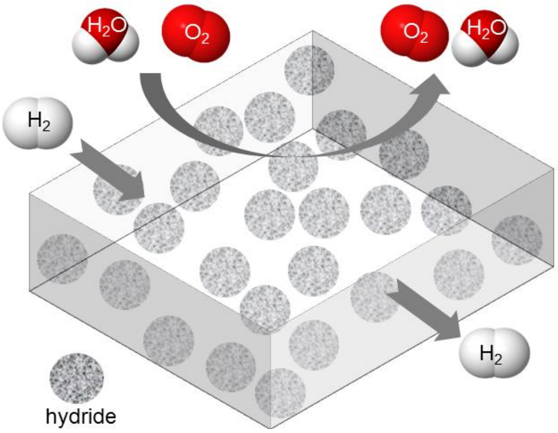

Figure 1. Schematic of the metal hydride-TPX composite for hydrogen storage

Experimental Details

Materials synthesis and film preparation

Magnesium amide, $Mg(NH_2)_2$ (> 95 %), was synthesized by the reaction of MgH_2 (Rockwood, Germany, 99%) with NH_3 at 330 °C. LiH (97 %) and $LiBH_4$ (95 %) were purchased from Alfa-Aesar and Sigma-Aldrich, Germany, respectively. $6Mg(NH_2)_2$-9LiH-$LiBH_4$ (LMBNH) and $Mg(NH_2)_2$-2LiH (LMNH) were ball milled for 36 h at 200 rpm using a Fritsch Pulverisette 6 classic line planetary mill under 50 bar of H_2, with a ball to powder ratio of 40:1. All the operations involving powder handling (including milling) were performed in a glovebox (MBraun, Germany) in argon atmosphere and the levels H_2O and O_2 were kept below 10 ppm to prevent contamination. Commercially available pellets of polymethylpentene TPX, type RT18, were provided from Mitsui Chemicals, INC., (Düsseldorf, Germany), and used as a matrix material for the hydrides LMBNH and LMNH. Cyclohexane (99.9%, Merck, Darmstadt, Germany), was used as a solvent for the polymer and dispersant for the metal hydride powders LMBNH and LMNH. The solvent was degassed before use and kept under argon atmosphere.

The composite film was prepared in three steps. Initially, the polymer TPX was dissolved in cyclohexane at 75 °C under argon atmosphere. After that, the polymer pellets were dissolved in the liquid, resulting in a viscous solution and then transferred into a glovebox. The metal hydrides (LMBNH and LMNH) and the TPX solution were mixed under vigorous stirring around 5 min under an argon atmosphere and finally, the mixture was cast on a glass substrate with the use of a doctor-blade. The gap used for the casting was 2000 μm. The cast film was dried in the glovebox and the solvent was trapped in a cooling trap system. The as-prepared films are labeled LMBNH-TPX and LMNH-TPX, respectively. The films produced were used for characterization without further drying. The final film thickness achieved for the casting process was approximately 300 μm.

Materials Characterization

Differential thermal analysis (DTA), as well as temperature programmed desorption-mass spectrometry (TPD-MS) measurements were carried out using a Netzsch STA 409 C and a Hiden Isochema Analytical HAL 201 Mass-Spectrometer combined system, with 50 mL min^{-1} argon flow. The samples were heated from room temperature (RT) to 300 and 350 °C for DTA and TPD-MS, respectively, with a heating rate of 2 °C min^{-1}.

High-pressure differential scanning calorimetry (HP-DSC) measurements were carried out using a Netzsch DSC 204 HP at hydrogen pressures of 1 bar and 80 bar, respectively. The samples were heated from RT to 200 °C for LMBNH and LMBNH-TPX, and 250 °C for LMNH and LMNH-TPX, with a heating rate of 5 and 2 °C min^{-1} for dehydrogenation and re-hydrogenation, respectively. The samples including TPX underwent another treatment RT up to 200 and 250 °C in two different ramps, with a heating rate of 5 °C min^{-1}.

The reversibility experiments were investigated using an in-house developed Sieverts-type apparatus (Sonja II, HZG, Germany), keeping the samples in isothermal conditions at 180 °C for LMBNH-based samples and 200 °C for LMNH-based samples under a hydrogen pressure of 1 bar for desorption and 80 bar for absorption, respectively. In addition, it was estimated that 12 hours are enough for handling and packaging these composites from synthesis inside a glovebox to their insertion into a hydrogen storage tank, therefore, the air-exposure time was chosen for 12 hours for all those air-exposure samples before conducting the cycling experiments.

In situ synchrotron radiation powder X-ray radiation diffraction (SR-PXRD) experiments were performed at the diffraction beamline P.02.1 in the PETRA III storage ring of the synchrotron facility “DESY”, in Hamburg, Germany. The fixed wavelength (λ) was 0.20716 Å and patterns were acquired with a PerkinElmer XRD1621 image detector (2048*2048 pixel, each of size 200*200 μm^2) and the distance from the sample to the detector was ca. 1470 mm. The powder was loaded into a quartz capillary tube and then fixed on an in-house developed *in situ* measuring cell (HZG, Germany), which was able to control heating temperatures and operating pressures and atmospheres. Dehydrogenation experiments were performed from RT to 200 and 250 °C for LMBNH-TPX and LMNH-TPX, with a heating rate of 10 °C min^{-1} under 1 bar of H_2. Hydrogenation was done from RT to 200 and 250 °C for LMBNH-TPX and LMNH-TPX under 80 bar of H_2 with a heating ramp of 5 °C min^{-1}. For the oxidation experiments (Figure S1), samples were exposed to atmospheric air for 1 h before loading, and then the data were recorded by *in situ* SR-PXRD for 30 min at 40 °C before heating to a higher temperature. The 2D images were integrated with the software FIT2D.[58] Quantitative analyses were performed using MAUD software implementing the Rietveld approach.[59, 60]

XRD tests were carried out using a D8 discover X-ray diffractometer (Bruker, Germany) with Cu Kα radiation (λ = 1.54184 Å, 50 kV, 1000 mA) at a scanning rate of 1 degree min^{-1}. Air-tight sample holders were used (Bruker, Germany) to prevent contamination of the sample.

Scanning electron microscopy (SEM) was employed to investigate the morphological structure of the LMNH-TPX composites using a Helios Nanolab 200 DualBeam microscope (FEI, Co., Netherlands). The samples for SEM experiments were mounted onto aluminum stubs with double-sided adhesive and coated with 8 nm platinum just prior to the measurements. The samples were exposed to air during this process for several minutes. In order to investigate the inner structure of the composites a fracture was induced on the surface of the LMNH-TPX composites.

The gas transport parameters were determined with the time-lag (variable pressure, constant volume) method at 30 °C and 1000 mbar feed pressure for the gases H_2, N_2, O_2, and for H_2O vapor near the saturation pressure. Detailed information about the time-lag method can be found in supporting information and Figure S2. In short, the method relies on maintaining a constant feed pressure and measuring the permeate pressure changing as a function of time due to the diffusion of gas molecules through the TPX film of known thickness as it is described elsewhere.[4, 61, 62].

Results and Discussion

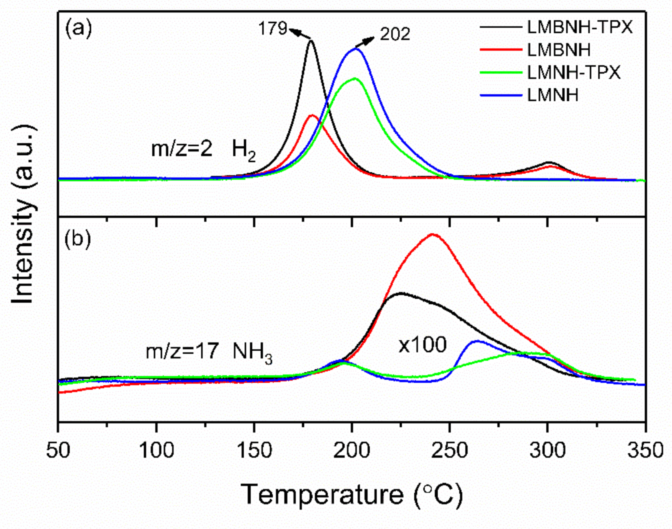

Figure 2. H_2-TPD-MS (a) and NH_3-TPD-MS (b) curves of LMBNH-TPX, LMBNH, LMNH-TPX and LMNH, respectively. Samples were heated from room temperature (RT) to 350 °C under 50 mL min^{-1} of argon flow with a heating rate of 2 °C min^{-1}.

The evolution of hydrogen and ammonia upon heating was monitored by TPD-MS experiments for all the investigated systems and the results are shown in Figure 2. As already reported in a previous work,[46] the addition of $LiBH_4$ lowers the decomposition peak temperature for the LMBNH composite to around 180 °C, which is more than 20 °C lower than that of the LMNH system (Figure 2(a)). After incorporation within the TPX matrix, the dehydrogenation properties of these metal hydride-TPX composites are completely relatable to those of the pure hydride systems (Figure 2(a)). LMBNH-TPX and LMBNH composites display the same onset (~ 130 °C) and peak temperatures (~ 179 °C). The onset and peak temperatures of LMNH-TPX and LMNH are 140 and 202 °C, respectively. In addition, the end temperatures of LMBNH-based and LMNH-based samples are ca. 200 and 250 °C, respectively. The NH_3-TPD-MS analysis (Figure 2(b)) shows that the release of ammonia from these composites depends only on the properties of the hydride systems. LMBNH and LMBNH-TPX have broad ammonia release peaks, which are likely due to the thermal decomposition of $Li_4(BH_4)(NH_2)_3$, a product of LMBNH-based composites, as shown in reaction (1).

$$6\ Mg(NH_2)_2 + 9\ LiH + LiBH_4 \leftrightarrow 3\ Li_2Mg_2(NH)_3 + Li_4(NH_4)(NH_2)_3 + 9\ H_2 \qquad (1)$$

In contrast to the LMBNH-based composites, the LMNH and LMNH-TPX systems exhibit two separate events for ammonia release. The first one at around 200 °C can be attributed to the multi-reaction mechanisms (solid-solid reaction mechanism and NH_3-mediated mechanism[63]), typical of amide-hydride systems. The second one is related to the decomposition of imides at high temperatures.[28]

DTA traces acquired for the four samples are displayed in Figure S3. The endothermic events below 200 °C match well with the release of H_2 observed in Figure 2(a). The LMBNH based samples have lower decomposition temperatures as compared to LMNH-based samples, while the LMNH based samples have both the main peak and the shoulder peak at ca. 186 and 197 °C, respectively. These can be ascribed to the two-steps reaction of the LMNH system (reactions 2-4).[42, 64]

$$2\ Mg(NH_2)_2 + 3\ LiH \leftrightarrow Li_2Mg_2(NH)_3 + 3\ H_2 + LiNH_2 \qquad (2)$$

$$Li_2Mg_2(NH)_3 + LiH + LiNH_2 \leftrightarrow 2\ Li_2Mg(NH)_2 + H_2 \qquad (3)$$

$$2\ Mg(NH_2)_2 + 4\ LiH \leftrightarrow 2\ Li_2Mg(NH)_2 + 4\ H_2 \qquad (4)$$

The small temperature differences between the thermal events and the observed gaseous species displayed in Figures S1 and 2 may originate from the distance (a 1.5 m heated capillary) that the gas released during the DTA analysis needs to pass before reaching the mass spectrometer.

There are two main DTA transitions above 200 °C for both the LMBNH and LMBNH-TPX composites; the first signal at about 210 °C and the second one at ca. 240 °C, as discussed in Figure 2 (b), could be attributed to the decomposition reaction of $Li_4(BH_4)(NH_2)_3$ and $Li_2Mg_2(NH)_3$. The peak related to the melting of the polymer matrix is at around 240 °C (Figure S3); however, this signal is not clearly visible in the curves of LMBNH-TPX and LMNH-TPX composites, due to the superimposition with imide decomposition process. Upon cooling, the polymer recrystallization in TPX mixtures can be easily identified at 211 °C. Based on what was analyzed and discussed about TPD-MS and DTA in the Figures 2 and S3, it can be concluded that the by-reaction and by-product (NH_3) occur at temperatures above 200 and 250 °C for LMBNH-based and LMNH-based samples, respectively. These results also show that, for the applied experimental conditions, the TPX matrix does not influence the dehydrogenation properties of LMBNH and LMNH composites.

To further investigate sorption properties of the composite materials, all the samples underwent one de/re-hydrogenation cycle. These measurements were carried out with a high-pressure DSC device and the results are summarized in Figure 3. The first cycle of LMBNH and LMBNH-TPX, shown in Figures 3(a) and (b), show highly comparable de/re-hydrogenation properties. Both materials exhibit a dehydrogenation peak temperature at 186 °C and an absorption peak at 165 °C. Apart from the melting and recrystallized temperatures of TPX, the thermal events shown in Figure 3(c) are the same for the LMNH and LMNH-TPX composites. LMNH and LMNH-TPX show identical absorption properties too.

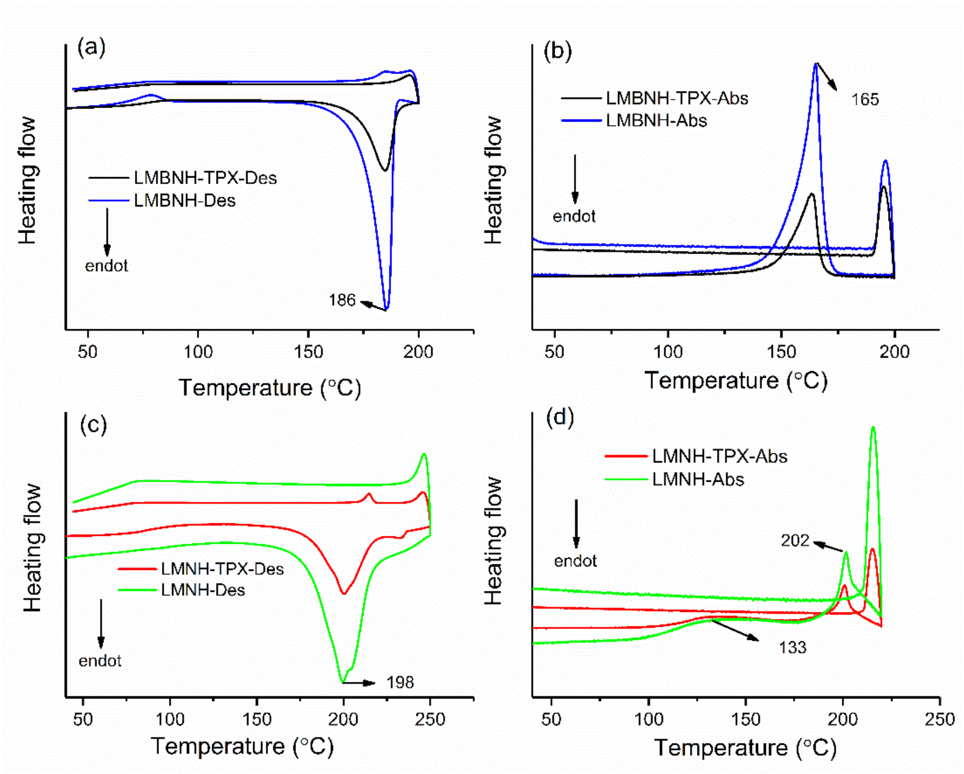

Figure 3. HP-DSC desorption (Des) measurements of LMBNH-TPX and LMBNH (a); HP-DSC absorption (Abs) measurements of LMBNH-TPX and LMBNH (b); HP-DSC desorption measurements of LMNH-TPX and LMNH (c); HP-DSC absorption measurements of LMNH-TPX and LMNH (d). HP-DSC desorption measurements were heated from RT to 200 °C and 250 °C with a heating rate of 5 °C min^{-1} under 1 bar of H_2, respectively for (a) and (c). HP-DSC absorption measurements were conducted under 80 bar of H_2 and heated from RT to 200 °C and 220 °C with a heating rate of 2 °C min^{-1}, respectively for (b) and (d).

Although these calorimetric studies of the de/re-hydrogenation reactions provide essential information regarding the similarities between the investigated systems, they do not provide detailed information on the mechanistic aspects of the reactions. For this reason, the de/re-hydrogenation reaction pathways have been investigated by means of the *in-situ* SR-PXRD experiments and the results are plotted in Figure 4. The starting diffraction pattern for the dehydrogenation of the LMBNH-TPX composite indicates the presence of the three phases $Mg(NH_2)_2$, LiH and TPX (Figure 4(a)). Upon heating to ca. 150 °C, the diffraction peaks of $Mg(NH_2)_2$ and LiH decrease, while simultaneously peaks of cubic $Li_2Mg(NH)_2$ appear. With a further increase of temperature to 185 °C, the peaks of TPX disappear, meaning that the TPX semicrystalline structure begins to melt and $Li_2Mg(NH)_2$ undergoes a polymorphic transition from cubic to orthorhombic at the same temperature. The diffraction peaks which are still present at 200 °C belong exclusively to the orthorhombic phase of $Li_2Mg(NH)_2$.

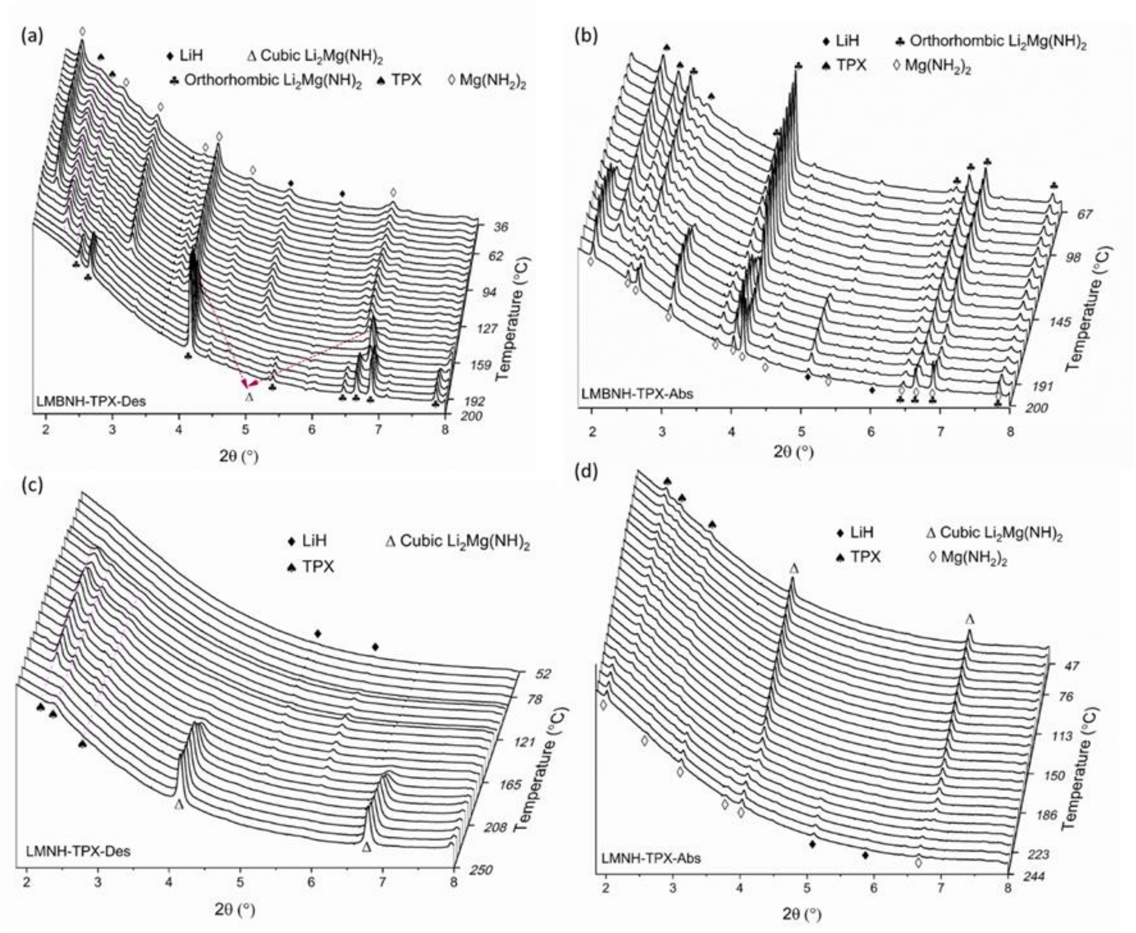

Figure 4. *In situ* SR-PXRD desorption (a) and absorption (b) of LMBNH-TPX; desorption (c) and absorption (d) of LMNH-TPX. In the desorption experiments (a) and (c), samples were heated from RT to 200 °C and 250 °C with a heating rate of 10 °C min^{-1} under 1 bar of H_2. In the absorption experiments (b) and (d), samples were under 80 bar of H_2 and heated from RT to 200 °C and 250 °C with a heating rate of 5 °C min^{-1}. All data were measured with $\lambda = 0.20716$ Å.

For the hydrogen absorption of LMBNH-TPX (Figure 4(b)), in the starting pattern and below 130 °C, the observed diffraction peaks can be assigned to TPX and orthorhombic $Li_2Mg(NH)_2$. The characteristic patterns of $Mg(NH_2)_2$ and LiH appear at ca. 140 °C and they can be seen until the end of this process, together with a bit of unreacted $Li_2Mg(NH)_2$. This trace of $Li_2Mg(NH)_2$

could be explained by taking into account that the reaction time for this *in situ* SR-PXD is not long enough to fully hydrogenate the material.

In contrast to the dehydrogenation pathway of LMBNH-TPX, $Mg(NH_2)_2$ is hardly observed during the entire dehydrogenation process of LMNH-TPX (Figure 4(c)). However, after hydrogenation, the diffraction peaks of $Mg(NH_2)_2$ can be identified as the primary phase along with LiH. The peaks of TPX disappear at the same temperature in the de/re-hydrogenation reactions of LMBNH-TPX and LMNH-TPX, while they appear again after those composites are cooled down after dehydrogenation (Figure 4(b) and (d)); DSC experiments show a similar behavior (Figure S4). This behavior of the polymer implies that, under the applied experimental and compositional conditions TPX is physically and chemically stable. The transformations of hydrides in the LMBNH-TPX and LMNH-TPX composites are the same as those in LMBNH and LMNH systems, which were reported in previous studies.[25, 27, 47, 65] One point to note is that $Li_4(NH_2)_3(BH_4)$ was not detected in the LMBNH-TPX system, possibly due to the use of cyclohexane. This may led to the formation of a thin layer of $LiBH_4$, which reacts with the *in situ* formed $LiNH_2$, producing a $Li_4(NH_2)_3(BH_4)$ layer as well.

In an effective attempt to study the stability against oxygen and moisture contamination of the air-exposed hydride-polymer composites, their de/re-hydrogenation were investigated over a span of several cycles. Figure 5 summarizes the data acquired from the de/re-hydrogenation cycles of LMBNH-TPX, the air-exposed LMBNH-TPX (shortened as LMBNH-TPX-O_2 hereafter), the pure LMBNH, and the air-exposed LMBNH (shortened as LMBNH-O_2 hereafter). The as prepared samples show excellent reversibility, with both maintaining their hydrogen capacities of ca. 4.0 wt% and 4.1 wt% for LMBNH-TPX and LMBNH, respectively. The hydrogen contents for these samples close to the previously reported value 4.2 wt%.[46] On the other hand, the air-exposed composites show a decrease of the hydrogen capacities.

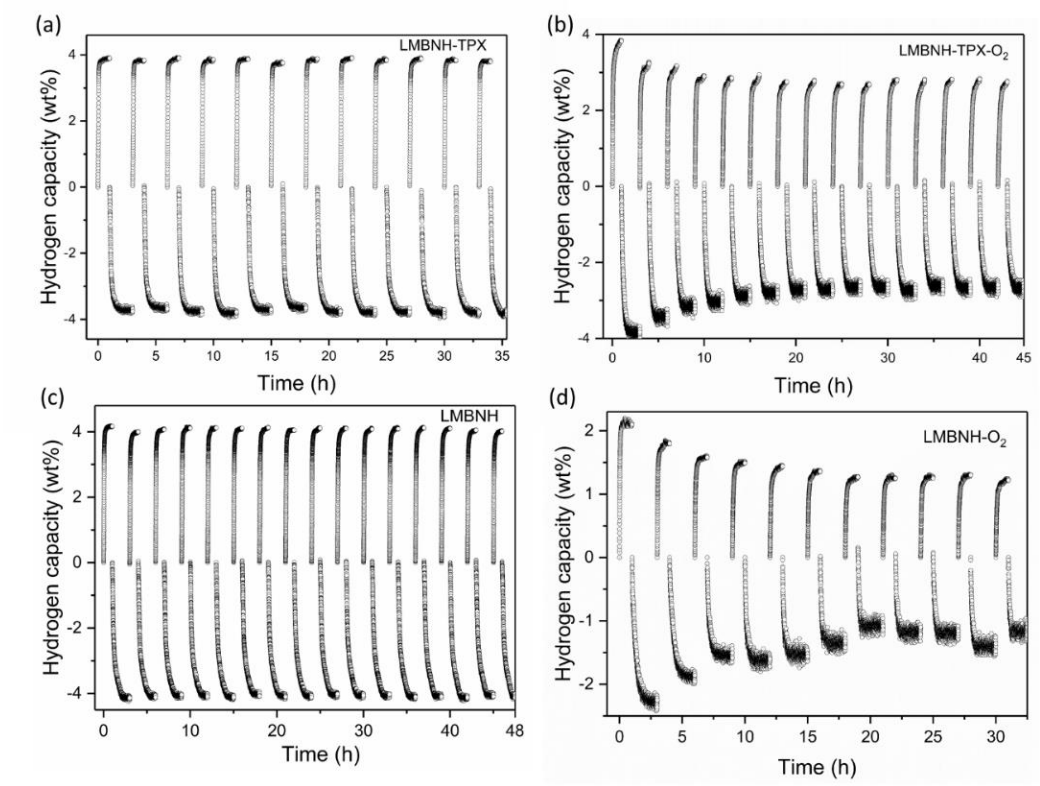

Figure 5. Reversibility of LMBNH-TPX (a); LMBNH-TPX-O_2 (air-exposed LMBNH-TPX) (b); LMBNH (c); and LMBNH-O_2 (air-exposed LMBNH) (d). Isothermal de/ab-sorption cycling experiments were performed at 180 °C and 1 and 80 bar for desorption and absorption, respectively. The hydrogen capacities of LMBNH-TPX and LMBNH-TPX-O_2 are just considered the hydride fraction.

In detail, the LMBNH-TPX system is more stable than the pure LMBNH system. The hydrogen capacity measured in the first cycle of the LMBNH-TPX-O_2 is the same as that of the as prepared LMBNH-TPX, meaning that at room temperature O_2 and or H_2O do not significantly affect the integrity of the material. During cycling, the hydrogen storage capacity drops continuously from the first to the fifth cycle; after the fifth cycle, the reversible H_2 content is stable at ca. 3.0 wt%. The reason behind this phenomenon could be the physisorption or physical adhesion of O_2 and/or H_2O on the surface of LMBNH-TPX, which later reacts with the hydrides to form metal oxides such as Li_2O and MgO. In comparison, the first cycle of the LMBNH-O_2 system shows an immediate drop in hydrogen capacity to ca. 2.0 wt%, which indicates that the material strongly reacted with O_2 and/or H_2O during air exposure. For this system, after 7 cycles, the hydrogen capacity stabilizes to ca. 1.5 wt%. The stabilization of both LMBNH-TPX-O_2 and LMBNH-O_2 observed from these cycling studies suggests that the polymer can effectively protect the hydrides and thus increase the stability and reversibility of the hydrogen storage for the composites.

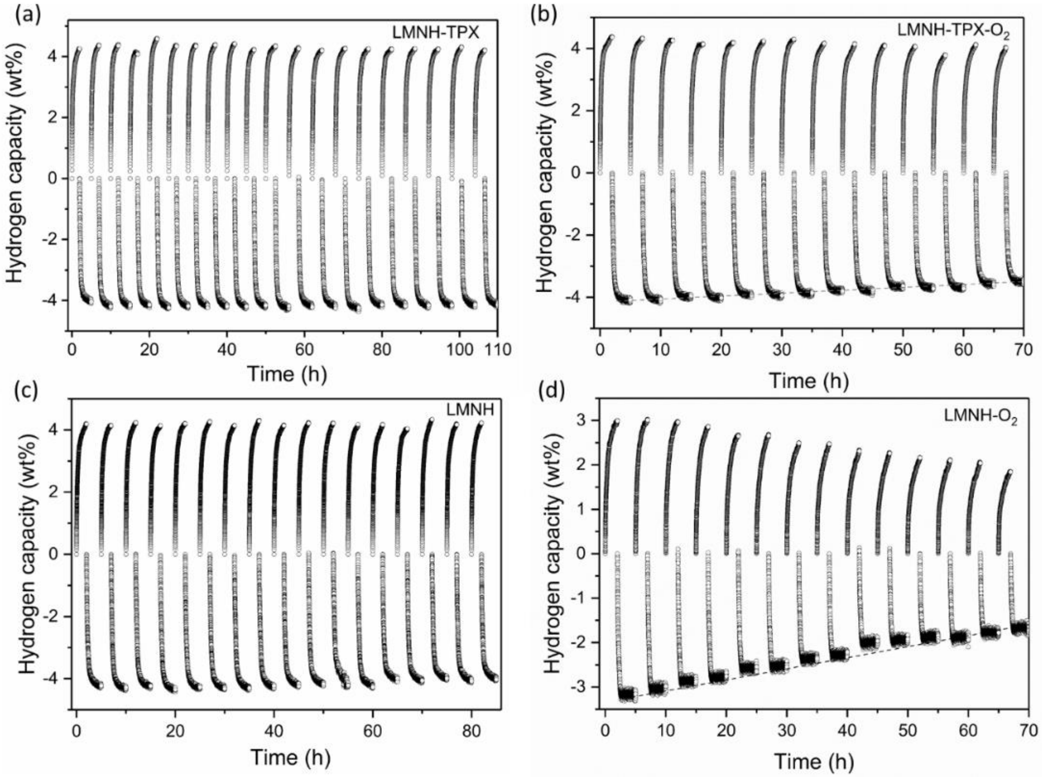

Figure 6. Reversibility of LMNH-TPX (a); LMNH-TPX-O_2 (air-exposed LMNH-TPX) (b); LMNH (c); and LMNH-O_2 (air-exposed LMNH) (d). Isothermal de/ab-sorption cycles were performed at 200 °C and 1 and 80 bar for desorption and absorption, respectively. The hydrogen capacities of LMNH-TPX and LMNH-TPX-O_2 are considered only the hydride fraction.

The reversibility of LMNH-TPX and LMNH after different treatments is summarized in Figure 6. Not only the as prepared LMNH-TPX, but also the air-exposed LMNH-TPX show significantly higher stability compared to the pristine LMNH systems. There is almost no H_2 content attenuation during the first 20 cycles in the as prepared LMNH-TPX system; however, the LMNH system starts to lose some capacity from the ninth cycle onwards. The higher material stability could be attributed to a confinement effect of the metal hydride in the TPX polymer matrix, which does not allow the sintering of the LMNH particles and consequently does not lead to a drop of hydrogen capacity and kinetic properties. The hydrogen capacities of LMNH-TPX and LMNH are ca. 4.3 wt%, considering the hydride fraction only. The cycled LMNH-TPX also underwent dehydrogenation at 250 °C and achieved a measured hydrogen capacity of 5.2 wt% which complies perfectly with previously reported results[27, 34] (Figure S5). The temperature, at 200 °C, is not high enough to release the hydrogen from the LMNH-based systems completely, which possibly explains the observed dehydrogenation values in Figures 6(a) and (c). Both samples exposed to air show a reduction in hydrogen capacity during cycling and the slope due to this decrease indicates that this effect is steeper for the LMNH-O_2 than that of LMNH-TPX-O_2. The calculated rates of reduction are 0.021 wt% (Figure 6(b)) and 0.1 wt% (Figure 6(d)) per cycle, for LMNH-TPX-O_2 and LMNH-O_2, respectively. The effect of atmospheric exposure in LMBNH-based and LMNH-based systems is slightly different. In this case, the H_2 content reduction subsides completely after several cycles in LMBNH-based systems; on the other hand, it continues with a rather constant rate during the cycles for LMNH-based systems. The reason behind this phenomenon could be the presence of the $LiBH_4$ film, which further limits O_2 and/or H_2O contamination.

XRD patterns of the samples before and after hydrogenation (Figures 5 and 6) are shown in Figure S6. After 12 h exposure to air, the diffraction peaks of Li_2O are observed in both LMBNH-TPX and LMBNH. Li_2O along with some unreacted $Li_2Mg(NH)_2$ is present in the hydrogenated samples. However, the peaks intensities of Li_2O and $Li_2Mg(NH)_2$ in the air-exposed LMBNH are much stronger than those in the air-exposed LMBNH-TPX system. Similar phenomena have also been observed in the LMNH-based system, where the Li_2O and MgO are present in the air-exposed LMNH composite (Figure S6(d)), but not in the air-exposed LMNH-TPX system (Figure S6(c)).

Unlike the other samples, all of the $Li_2Mg(NH)_2$ reacts with hydrogen to form $Mg(NH_2)_2$ and LiH in the system of LMNH-TPX (Figure S6(c)). It should be pointed out that traces of Li_2O found in the hydrogenated LMBNH-TPX and LMNH-TPX composites could be due to contamination from the reactor. The XRD results are in agreement with the hydrogen reversibility properties shown in Figures 5 and 6.

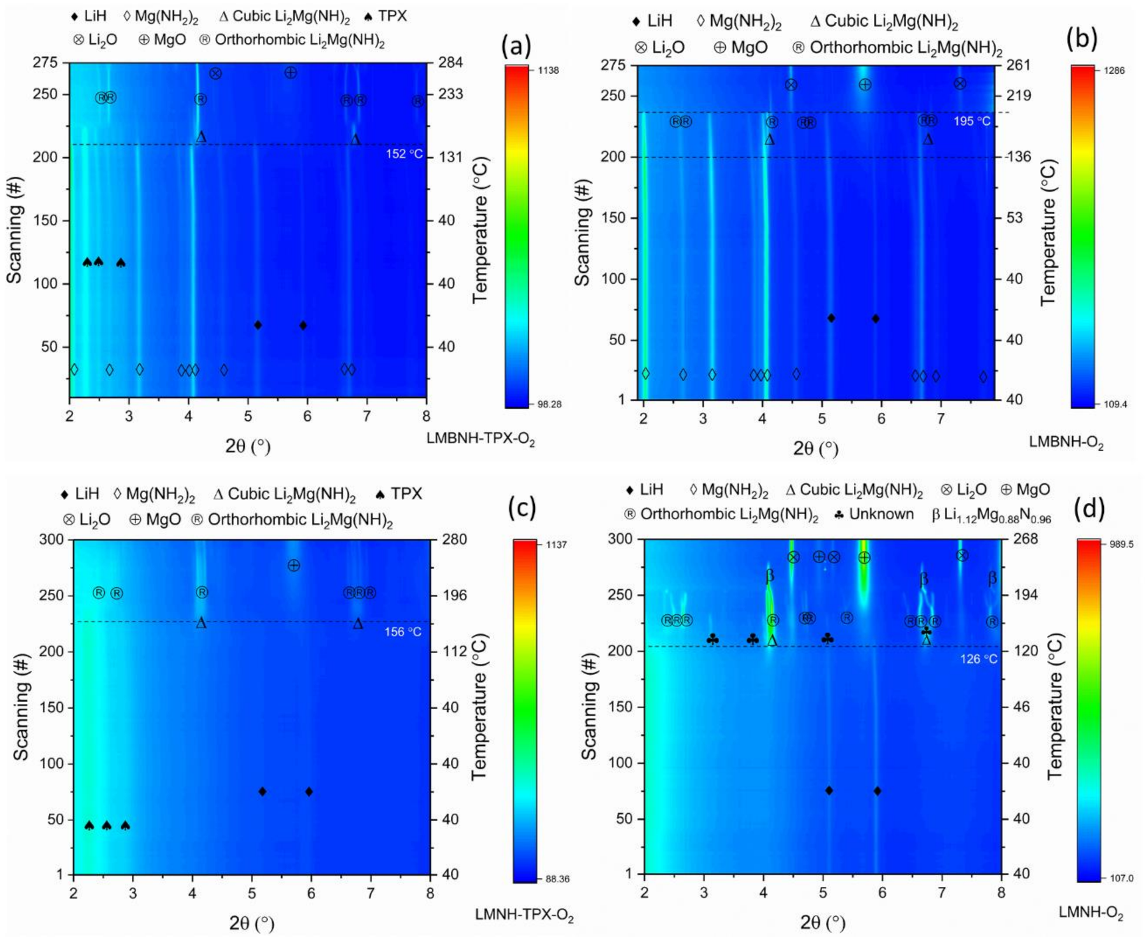

Figure 7. *In situ* SR-PXRD desorption of LMBNH-TPX (a); LMBNH (b); LMNH-TPX (c) and LMNH (d) under air. The samples have been exposed to air for 1 h prior to the measurements. Samples were held isothermally at 40 °C for 30 min before being heated to 300 °C with a heating rate of 10 °C min^{-1}. All data were measured with $\lambda = 0.20716$ Å.

In situ SR-PXRD experiments were used to investigate the desorption reaction of the air-exposed hydride-TPX composites (Figure 7). All of them have been exposed to air for 1 h before loading them into the *in situ* cell (Figure S1), and then they were kept at 40 °C for 30 min before heating to high temperatures. Figure 7 shows little evidence of oxidation before heating to high temperatures. The results reported in Figure 7(a) are in very close agreement with the measurement reported in Figure 4(a). $Mg(NH_2)_2$ and LiH are stable up to 152 °C, and then they react with each other to form cubic $Li_2Mg(NH)_2$, as shown in reaction 4. By increasing temperature, the diffraction peaks of TPX disappear and $Li_2Mg(NH)_2$ changes from cubic to orthorhombic structure. Finally, some weak peaks of MgO and Li_2O appear at about 280 °C. This is different to the LMBNH-TPX composite where only traces of $Li_2Mg(NH)_2$ are observed at temperatures below 190 °C in the LMBNH system (Figure 7(b)), and a small amount of MgO is visible at ca. 140 °C. As expected, the peaks of Li_2O and MgO are visible at temperatures above 195 °C. This clearly indicates that the thermal dehydrogenation reactions of LMBNH in air and H_2 atmosphere are different. Figure 7(c) shows that $Mg(NH_2)_2$ reacts with LiH to form cubic $Li_2Mg(NH)_2$ at ca. 156 °C in LMNH-TPX, and $Li_2Mg(NH)_2$ undergoes its polymorphic change from cubic to orthorhombic structure at around 200 °C. In addition, MgO starts to form at 160 °C. In Figure 7(d), $Mg(NH_2)_2$ reacts with LiH to form cubic $Li_2Mg(NH)_2$ together with unknown phases at temperatures below 126 °C which is 30 °C lower than in the experiments presented in Figures 7(a) and (c). At the same time, the diffraction peaks of Li_2O and MgO appear. Upon increasing the temperature to ca. 160 °C the polymorph of $Li_2Mg(NH)_2$ changes from the cubic to the orthorhombic. The formation of Li_2O and MgO affects the ratio of Li to Mg in the imide and nitride, and a non-equilibrium stoichiometry $Li_{1.12}Mg_{0.88}N_{0.96}$ is formed at the temperature above 200 °C. Finally, all the Li and Mg change to their oxides. This indicates that the reactions between $Mg(NH_2)_2$ and LiH are influenced by exposure to air. As a result of studying these materials, the following reactions 5-8 are proposed:

$$2\ LiH + H_2O \rightarrow 2\ H_2 + Li_2O \qquad (5)$$

$$4\ LiH + O_2 \rightarrow 2\ H_2 + 2Li_2O \qquad (6)$$

$$Mg(NH_2)_2 + H_2O \rightarrow 2\ NH_3 + MgO \qquad (7)$$

$$NH_3 + LiH \rightarrow LiNH_2 + H_2 \qquad (8)$$

These results show that the hydride composites are more air sensitive than the hydride-TPX composites. O_2 and H_2O from exposure to atmosphere affect the reactions between $Mg(NH_2)_2$ and LiH leading to the observed reduction of hydrogen storage capacity (Figures 5 and 6). Irrespective of the atmosphere under which the reactions are carried out (*i.e.*, H_2 or air), the material exposed to air for ca. 90 min has similar reaction pathways for the hydride-TPX composites.

As a representative composite, the system LMNH-TPX after 20 cycles of de/re-hydrogenations (Figure 6) was studied by SEM to analyze the morphology of the hydride-TPX composites (Figure 8). Figure 8(a) shows that the surface of the TPX polymer covers the whole surface of the LMNH and holds the particles stable after the cycling experiments. To investigate whether the same effect is visible in the bulk structure of the composites a fracture was induced on the surface of the LMNH-TPX (Figure 8b). The SEM images of the fracture (Figure 8b-d) indicate that the three-dimensional network structure of the cycled LMNH-TPX is the same as at the surface; the LMNH is uniformly distributed within the TPX.

To understand the stability of the metal hydride particles in the polymer matrix, it is necessary to comment on the gas transport properties of the polymer. The diffusion coefficient of O_2 and H_2O in TPX are 1.56×10^{-10} [m^2/s] and 1.59×10^{-12} [m^2/s] at 30 °C (see Table S1), as determined by time-lag experiments with pure gases. The value of water solubility coefficient for TPX is indeed higher than that for other gases, but since the water vapour diffusion coefficient is very low the water is not passing through the polymer film rapidly, meaning that the process is controlled by the diffusion. In case of the hydrogen storage composites that means that water does not reach the particles as easily as it would have been if the particles were directly exposed to air. It is understood from the low solubility values that during exposure in air atmosphere, the contact between hydrides and gases such as O_2 and H_2O is hindered by the TPX matrix. That is the reason why the hydride-TPX composites exposed to air demonstrate initially and maintain both an excellent reaction stability (Figure 7) and reversibility (Figures 5 and 6). Also the high diffusion coefficient for hydrogen, which is equal to 20.7×10^{-10} [m^2/s] at 30 °C, indicates that the polymer allows hydrogen to reach the metal hydrides fast.

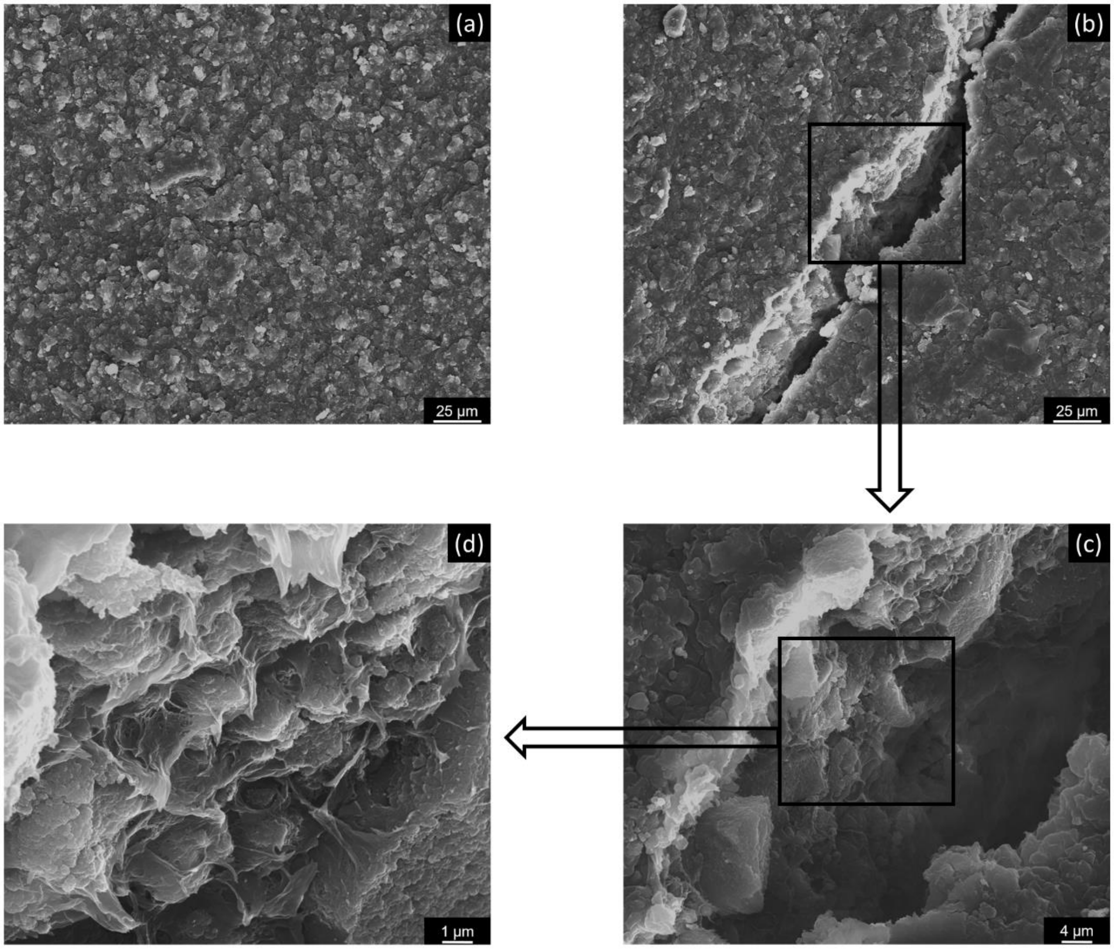

Figure 8. SEM images of the 20-times cycled LMNH-TPX composite: (a) surface, (b) fracture induced on the surface and (c and d) higher magnifications of the fractured area.

Conclusion

LMBNH-TPX, LMNH-TPX composites have been prepared by casting the mixture of LMBNH and LMNH within the TPX matrix on a glass substrate using a doctor-blade technique. Hydrogen storage properties and reaction mechanisms of these composites under air and H_2 atmosphere are studied. *In situ* SR-PXRD reveals that both LMBNH-TPX and LMNH-TPX show significantly enhanced air-stabilities as compared to the pure LMBNH and LMNH. After exposing to air for 12 hours, the reversible hydrogen capacities of LMBNH-TPX and LMNH-TPX in the tenth cycle are ca. 3.0 and 4.0 wt%, respectively, which are two-times higher than those of LMBNH (1.5 wt%) and LMNH (2.0 wt%) when exposed to the same conditions. The reduction rate of reversible hydrogen capacity of LMNH-TPX after exposing to air is 0.021 wt% per cycle. However, that value is 5 times larger (0.1 wt% per cycle) for pure LMNH. The hydrogen storage properties of these composites are dependent on the hydrides and not on the presence of the polymer matrix. Both LMBNH-TPX and LMNH-TPX retain the same loading capacities and kinetic properties, while the latter exhibits improved reversibility. SEM analysis confirms that the metal hydrides remain embedded in the polymeric matrix even after a number of cycles as proposed in Figure 1, and the three-dimensional integrity has been retained in both types of composites. The results detailed here show that the polymer provides an excellent barrier for the hydrides, avoiding direct contact with oxygen or water, therefore increasing the reversibility lifetime significantly and suppressing the sintering effects of the metal hydrides during hydrogenation and dehydrogenation reactions at this temperature. The present study therefore demonstrates a suitable way to fabricate air-stable metal hydride-polymer composite for hydrogen storage applications.

Acknowledgements

We gratefully acknowledge financial support from the Federal Ministry of Education and Research of Germany (BMBF) via the project HyScore (FKZ: 03SF0532A-D). We appreciate the access to the beam line P02.1 at the PETRA III synchrotron (DESY, Germany), and thank the Helmholtz Energy Materials Characterization platform for access to the equipment which is financially supported by The Helmholtz Association. We would also like to acknowledge Prof. Erica Lilleodden and Dr. Henry Ovri from the Department of Experimental Materials Mechanics, Institute of Materials Research at the Helmholtz-Zentrum Geesthacht, for access to the SEM and support during the SEM investigations. Last but not least, we would like to gratefully acknowledge Dr. Sergey Shishatskiy and Mr. Jan Wind for contributing to the polymer selection and for experimental support, as well as the company Mitsui Chemicals, INC. (Düsseldorf, Germany) for kindly providing the polymer for our research purposes.

References

[1] D. Gay, Composite materials: design and applications, CRC press, 2014.

[2] A. Dreyer, A. Feld, A. Kornowski, E.D. Yilmaz, H. Noei, A. Meyer, T. Krekeler, C. Jiao, A. Stierle, V. Abetz, H. Weller, G.A. Schneider, Nature Materials, 15 (2016) 522-528.

[3] P. Georgopanos, E. Eichner, V. Filiz, U.A. Handge, G.A. Schneider, S. Heinrich, V. Abetz, Composites Science and Technology, 146 (2017) 73-82.

[4] F. Weigelt, P. Georgopanos, S. Shishatskiy, V. Filiz, T. Brinkmann, V. Abetz, Polymers, 10 (2018) 51.

[5] P. Georgopanos, G.A. Schneider, A. Dreyer, U.A. Handge, V. Filiz, A. Feld, E.D. Yilmaz, T. Krekeler, M. Ritter, H. Weller, V. Abetz, Scientific Reports, 7 (2017) 7314.

[6] P.N. Dyachenko, S. Molesky, A.Y. Petrov, M. Störmer, T. Krekeler, S. Lang, M. Ritter, Z. Jacob, M. Eich, Nature Communications, 7 (2016) 11809.

[7] R. Hadal, Q. Yuan, J.P. Jog, R.D.K. Misra, Materials Science and Engineering a-Structural Materials Properties Microstructure and Processing, 418 (2006) 268-281.

[8] A. Dorigato, A. Pegoretti, Polymer International, 59 (2010) 719-724.

[9] J.M. Cannata, J.A. Williams, L.Q. Zhang, C.H. Hu, K.K. Shung, Ieee Transactions on Ultrasonics Ferroelectrics and Frequency Control, 58 (2011) 2202-2212.

[10] G. Barkhordarian, T. Klassen, M. Dornheim, R. Bormann, Journal of Alloys and Compounds, 440 (2007) L18-L21.

[11] U. Bösenberg, J.W. Kim, D. Gosslar, N. Eigen, T.R. Jensen, J.M.B. von Colbe, Y. Zhou, M. Dahms, D.H. Kim, R. Günther, Y.W. Cho, K.H. Oh, T. Klassen, R. Bormann, M. Dornheim, Acta Materialia, 58 (2010) 3381-3389.

[12] C. Pistidda, G. Barkhordarian, A. Rzeszutek, S. Garroni, C.B. Minella, M.D. Baró, P. Nolis, R. Bormann, T. Klassen, M. Dornheim, Scripta Materialia, 64 (2011) 1035-1038.

[13] L.H. Jepsen, M.B. Ley, Y.-S. Lee, Y.W. Cho, M. Dornheim, J.O. Jensen, Y. Filinchuk, J.E. Jørgensen, F. Besenbacher, T.R. Jensen, Materials Today, 17 (2014) 129-135.

[14] N. Bergemann, C. Pistidda, C. Milanese, T. Emmler, F. Karimi, A.L. Chaudhary, M.R. Chierotti, T. Klassen, M. Dornheim, Chemical Communications, 52 (2016) 4836-4839.

[15] T.-T. Le, C. Pistidda, J. Puszkiel, M.V. Castro Riglos, F. Karimi, J. Skibsted, S.P. GharibDoust, B. Richter, T. Emmler, C. Milanese, A. Santoru, A. Hoell, M. Krumrey, E. Gericke, E. Akiba, T.R. Jensen, T. Klassen, M. Dornheim, The Journal of Physical Chemistry C, 122 (2018) 7642-7655.

[16] R. Gosalawit−Utke, T.K. Nielsen, K. Pranzas, I. Saldan, C. Pistidda, F. Karimi, D. Laipple, J. Skibsted, T.R. Jensen, T. Klassen, M. Dornheim, The Journal of Physical Chemistry C, 116 (2012) 1526-1534.

[17] P. Chen, Z. Xiong, J. Luo, J. Lin, K.L. Tan, Nature, 420 (2002) 302-304.

[18] P. Chen, M. Zhu, Materials Today, 11 (2008) 36-43.

[19] S.-i. Orimo, Y. Nakamori, J.R. Eliseo, A. Zu, C.M. Jensen, Materials Research, (2007).

[20] J. Yang, A. Sudik, C. Wolverton, D.J. Siegel, Chemical Society Reviews, 39 (2010).

[21] H.J. Cao, Y. Zhang, J.H. Wang, Z.T. Xiong, G.T. Wu, P. Chen, Progress in Natural Science-Materials International, 22 (2012) 550-560.

[22] L.E. Klebanoff, J.O. Keller, International Journal of Hydrogen Energy, 38 (2013) 4533-4576.

[23] C. Liang, Y. Liu, H. Fu, Y. Ding, M. Gao, H. Pan, Journal of Alloys and Compounds, 509 (2011) 7844-7853.

[24] S. Garroni, A. Santoru, H. Cao, M. Dornheim, T. Klassen,
C. Milanese, F. Gennari and C. Pistidda, Energies 2018, 11, 1027; doi:10.3390/en11051027

[25] Z.T. Xiong, G.T. Wu, H.J. Hu, P. Chen, Advanced Materials, 16 (2004) 1522-+.

[26] Y. Nakamori, G. Kitahara, S. Orimo, Journal of Power Sources, 138 (2004) 309-312.

[27] W. Luo, Journal of Alloys and Compounds, 381 (2004) 284-287.

[28] H.Y. Leng, T. Ichikawa, S. Hino, N. Hanada, S. Isobe, H. Fujii, The Journal of Physical Chemistry B, 108 (2004) 8763-8765.

[29] Z.T. Xiong, J.J. Hu, G.T. Wu, P. Chen, W.F. Luo, K. Gross, J. Wang, Journal of Alloys and Compounds, 398 (2005) 235-239.

[30] G.L. Xia, X.W. Chen, C.F. Zhou, C.F. Zhang, D. Li, Q.F. Gu, Z.P. Guo, H.K. Liu, Z.W. Liu, X.B. Yu, Journal of Materials Chemistry A, 3 (2015) 12646-12652.

[31] L. Xie, Y. Liu, G. Li, X. Li, The Journal of Physical Chemistry C, 113 (2009) 14523-14527.

[32] H.J. Cao, H. Wang, C. Pistidda, C. Milanese, W.J. Zhang, A.L. Chaudhary, A. Santoru, S. Garroni, J. Bednarcik, H.P. Liermann, P. Chen, T. Klassen, M. Dornheim, Physical Chemistry Chemical Physics, 19 (2017) 8457-8464.

[33] H.J. Cao, Y. Zhang, J.H. Wang, Z.T. Xiong, G.T. Wu, J.S. Qiu, P. Chen, Dalton Transactions, 42 (2013) 5524-5531.

[34] H.J. Cao, H. Wang, T. He, G.T. Wu, Z.T. Xiong, J.S. Qiu, P. Chen, Rsc Advances, 4 (2014) 32555-32561.

[35] S. Qiu, X. Ma, E. Wang, H. Chu, J. Huot, Y. Zou, C. Xiang, F. Xu, L. Sun, Journal of Alloys and Compounds, 704 (2017) 44-50.

[36] H.-J. Lin, H.-W. Li, B. Paik, J. Wang, E. Akiba, Dalton Transactions, 45 (2016) 15374-15381.

[37] J.J. Hu, M. Fichtner, P. Chen, Chemistry of Materials, 20 (2008) 7089-7094.

[38] H. Wang, G.T. Wu, H.J. Cao, C. Pistidda, A.L. Chaudhary, S. Garroni, M. Dornheim, P. Chen, Advanced Energy Materials, 7 (2017).

[39] H. Wang, H.J. Cao, C. Pistidda, S. Garroni, G.T. Wu, T. Klassen, M. Dorheim, P. Chen, Chemistry-an Asian Journal, 12 (2017) 1758-1764.

[40] M. Baricco, M. Bang, M. Fichtner, B. Hauback, M. Linder, C. Luetto, P. Moretto, M. Sgroi, Journal of Power Sources, 342 (2017) 853-860.

[41] H. Pan, S. Shi, Y. Liu, B. Li, Y. Yang, M. Gao, Dalton Transactions, 42 (2013) 3802-3811.

[42] J. Wang, T. Liu, G. Wu, W. Li, Y. Liu, C.M. Araújo, R.H. Scheicher, A. Blomqvist, R. Ahuja, Z. Xiong, P. Yang, M. Gao, H. Pan, P. Chen, Angewandte Chemie International Edition, 48 (2009) 5828-5832.

[43] T. Durojaiye, J. Hayes, A. Goudy, Journal of Physical Chemistry C, 117 (2013) 6554-6560.

[44] C. Li, Y.F. Liu, Y.J. Gu, M.X. Gao, H.G. Pan, Chemistry-an Asian Journal, 8 (2013) 2136-2143.

[45] C. Li, Y. Liu, R. Ma, X. Zhang, Y. Li, M. Gao, H. Pan, ACS Applied Materials & Interfaces, 6 (2014) 17024-17033.

[46] H.J. Cao, G.T. Wu, Y. Zhang, Z.T. Xiong, J.S. Qiu, P. Chen, Journal of Materials Chemistry A, 2 (2014) 15816-15822.

[47] H. Cao, W. Zhang, C. Pistidda, J. Puszkiel, C. Milanese, A. Santoru, F. Karimi, M.V. Castro Riglos, G. Gizer, E. Welter, J. Bednarcik, M. Etter, P. Chen, T. Klassen, M. Dornheim, Physical Chemistry Chemical Physics, 19 (2017) 32105-32115.

[48] S. Börries, O. Metz, P.K. Pranzas, J.M. Bellosta von Colbe, T. Bücherl, M. Dornheim, T. Klassen, A. Schreyer, Journal of Power Sources, 328 (2016) 567-577.

[49] F. Sun, M.Y. Yan, X.P. Liu, J.H. Ye, Z.N. Li, S.M. Wang, L.J. Jiang, International Journal of Hydrogen Energy, 40 (2015) 6173-6179.

[50] W. Luo, J. Wang, K. Stewart, M. Clift, K. Gross, Journal of Alloys and Compounds, 446-447 (2007) 336-341.

[51] J.G. Yuan, Y.F. Zhu, L.Q. Li, Y. Wu, S.X. Zhou, International Journal of Hydrogen Energy, 42 (2017) 22366-22372.

[52] K.-J. Jeon, H.R. Moon, A.M. Ruminski, B. Jiang, C. Kisielowski, R. Bardhan, J.J. Urban, Nat Mater, 10 (2011) 286-290.

[53] P.E. de Jongh, Nat Mater, 10 (2011) 265-266.

[54] M. Pentimalli, F. Padella, A. La Barbera, L. Pilloni, E. Imperi, Energy Conversion and Management, 50 (2009) 3140-3146.

[55] R. Pedicini, B. Schiavo, P. Rispoli, A. Saccà, A. Carbone, I. Gatto, E. Passalacqua, Energy, 64 (2014) 607-614.

[56] Z. Kurban, A. Lovell, S.M. Bennington, D.W.K. Jenkins, K.R. Ryan, M.O. Jones, N.T. Skipper, W.I.F. David, The Journal of Physical Chemistry C, 114 (2010) 21201-21213.

[57] J.G. Zhang, Y.F. Zhu, H.J. Lin, Y.N. Liu, Y. Zhang, S.Y. Li, Z.L. Ma, L.Q. Li, Advanced Materials, 29 (2017).

[58] A. Hammersley, European Synchrotron Radiation Facility Internal Report ESRF97HA02T 1997, 68.

[59] L. Lutterotti, M. Bortolotti, G. Ischia, I. Lonardelli, H.R. Wenk, Zeitschrift Fur Kristallographie, (2007) 125-130.

[60] I. Lonardelli, H.R. Wenk, L. Lutterotti, M. Goodwin, Journal of Synchrotron Radiation, 12 (2005) 354-360.

[61] D. Pye, H. Hoehn, M. Panar, Journal of Applied Polymer Science, 20 (1976) 1921-1931.

[62] S. Shishatskiy, C. Nistor, M. Popa, S.P. Nunes, K.V. Peinemann, Advanced Engineering Materials, 8 (2006) 390-397.

[63] T. Ichikawa, N. Hanada, S. Isobe, H. Leng, H. Fujii, J. Phys. Chem. B, 108 (2004) 7887-7892.

[64] J. Hu, Y. Liu, G. Wu, Z. Xiong, P. Chen, The Journal of Physical Chemistry C, 111 (2007) 18439-18443.

[65] J. Rijssenbeek, Y. Gao, J. Hanson, Q. Huang, C. Jones, B. Toby, Journal of Alloys and Compounds, 454 (2008) 233-244.

Supporting information

Air-stable metal hydride-polymer composites of $Mg(NH_2)_2$-LiH and TPX™

Hujun Cao,[a]* Prokopios Georgopanos,[b]* Giovanni Capurso,[a] Claudio Pistidda,[a] Fynn Weigelt,[b] Anna-Lisa Chaudhary,[a] Volkan Filiz,[b] Jo-Chi Tseng,[c] Michael T. Wharmby,[c] Martin Dornheim[a] Volker Abetz,[b, d] and Thomas Klassen[a, e]

a. Institute of Materials Research, Materials Technology, Helmholtz-Zentrum Geesthacht GmbH, Max-Planck-Straße 1, 21502, Geesthacht, Germany.
E-Mail: hujun.cao@hzg.de; Fax: + 49 04152 / 87-2625; Tel: +49 04152 / 87-2643
b. Institute of Polymer Research, Helmholtz-Zentrum Geesthacht GmbH, Max-Planck-Straße 1, 21502, Geesthacht, Germany.
E-Mail: prokopios.georgopanos@hzg.de; Fax: + 49 04152 / 87-2466; Tel: +49 04152 / 87-2420
c. Deutsches Elektronen-Synchrotron (DESY), Notkestraße 85, 22607 Hamburg, Germany
d. Institute of Physical Chemistry, University of Hamburg, Martin-Luther-King-Platz 6, 20146 Hamburg, Germany.
e. Institute of Materials Technology, Helmut Schmidt University, Holstenhofweg 85, 22043 Hamburg, Germany.

Time-lag method for the estimation of the gas transport properties:

In short, the TPX film was placed into the measurement cell and sealed with a Viton® O-ring. The sealed membrane served as a barrier between the feed and permeate sides of the measurement instrumentation. Prior to the measurement, the apparatus was thoroughly evacuated. The pressure increase in the permeate chamber with known constant volume was monitored from the moment the gas was brought in contact with the membrane under a constant pressure. From the obtained curve, the time-lag, θ, was determined by extrapolating the slope of the linear increase to its intersection with the time axis and the gas permeability coefficient of the membrane was calculated from the linear part of the curve.[S1] The schematic representation of the experimental result is depicted in Figure S2. The diffusion coefficient of component *i* ($D_{eff,i}$) was calculated by the following equation [S2]: $\theta = \frac{l^2}{6\,D_{eff,i}}$, where *l* is the membrane film thickness and D_{eff} the effective diffusion coefficient of the penetrant in the studied material. The permeability ($P_{eff,i}$) is the function of: a) slope (i.e. dp/dt) of the linear part of the curve (Figure S2); b) driving force, derived from the difference of the feed and permeate pressure at the moment the slope is determined; c) membrane area exposed to the gas and d) membrane thickness. Knowing the volume of the permeate side of the measurement instrumentation and assuming that in the pressure range 0-10 mbar in which permeate pressure is acquired the gas in the permeate side can be considered as ideal, the ideal gas law helps to convert the pressure change into the gas volume change (i.e. dV/dt). Knowing all the aforementioned parameters the permeability coefficient can be determined. The solubility ($S_{eff,i}$) coefficient can be calculated from the following equation $\mathrm{P}_{eff,i} = \mathrm{D}_{eff,i}\,\mathrm{S}_{eff,i}$.

For the time-lag measurements, a custom-made machine was used. The gases used for the experiments (Linde AG, Munich, Germany) were of high purity, while a thermostat was used to maintain the temperature. The vacuum was generated by a turbomolecular pump (Pfeiffer GmbH, Asslar, Germany). A LabView (National Instruments, Austin, TX, USA) based custom software was used for the control of the time-lag experimental instrumentation as well as for the evaluation of the data. It should be noted that the placement of the Viton® O-ring involves relatively hard pressing of the O-ring onto the membrane. The O-ring has a 65 Shore hardness. The pressing ensures a good sealing of the membrane in the measurement cell. The accuracy of the method is based on the time measurement of the time-lag, which is measured with systematic error of 35±5 ms, rising from the speed of opening of the pneumatic KF16 vacuum valves. The precision of the permeability coefficient determination is ensured by: a) the thorough evacuation of the membrane before it is exposed to the gas under investigation; b) the careful calibration of the permeate volume (45.8±0.1 cm^3), and c) the use of highly accurate pressure sensors on the permeate side of the measurement instrumentation (Baratron 622 and 121 absolute capacitance manometers, 10 Torr range, MKS Inc., USA)For measurements of water as pure gas, the water used was Millipore deionized water (0.055 μS/cm) thoroughly degassed before use by repeated flash evacuation. The water was poured into a special stainless steel reservoir inside the thermostated zone of the time-lag instrumentation, kept at the same temperature as for the whole instrumentation. The experiment with the water vapour started with thorough evacuation of the membrane and feed gas reservoir. After satisfactory evacuation the measurement cell was closed and the feed gas reservoir was connected to the liquid water containing reservoir by opening of vacuum valves. The liquid water was allowed to evaporate until stable pressure was reached. In case the pressure was exceeding the saturated vapour pressure at the temperature of the thermostated measurement instrumentation, the measurement had to be aborted and liquid water was to be degassed again. Following this step, the feed gas and liquid water reservoirs were closed and the vacuum part evacuated to at least 10^{-3} mbar, the pressure in the permeate part was controlled to be not rising, and the measurement started by opening vacuum pneumatic valves, connecting feed gas reservoir and the feed side of the measurement cell. Obviously, at this time the pressure of the water vapour dropped due to the expansion into bigger volume. It means that the measurement of water vapour transport through the membrane cannot be done at water vapour activity close to unity which has double effect: disadvantage of not knowing behavior of the studied membrane at saturated water vapour conditions; and advantage of avoiding any possibility of water vapour condensation on the film surface by, e.g., Joule-Thomson effect. After experiments with the water vapour the vacuum system was flashed with nitrogen and evacuated repeatedly to avoid any gas contamination with water.

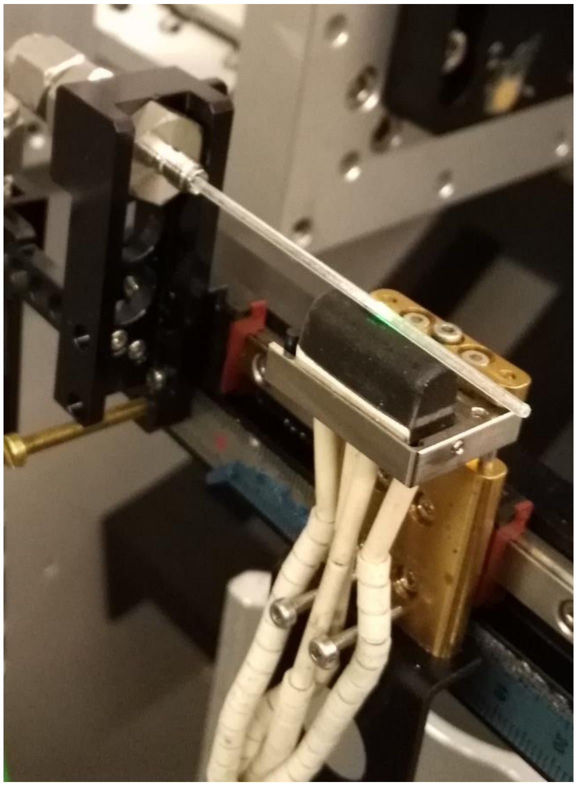

Figure S1. The digital photo of the setup for oxidation experiments, samples were loaded in the capillary, exposed to the air, and then heated to the high temperature.

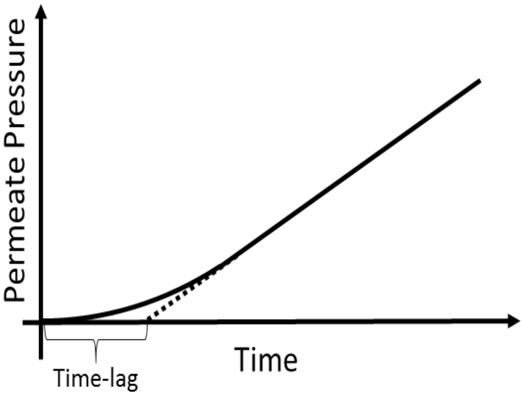

Figure S2. Schematic representation of the experimental result of the time-lag method for the estimation of the gas transport properties of the polymer film.

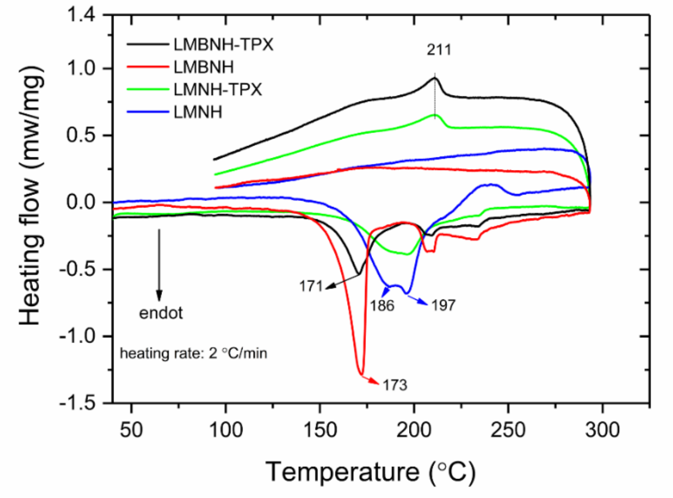

Figure S3. DTA curves of LMBNH-TPX, LMBNH, LMNH-TPX and LMNH, respectively. All the samples have been heated from RT to 300 °C under 50 mL min^{-1} of argon flow with a heating rate of 2 °C min^{-1}.

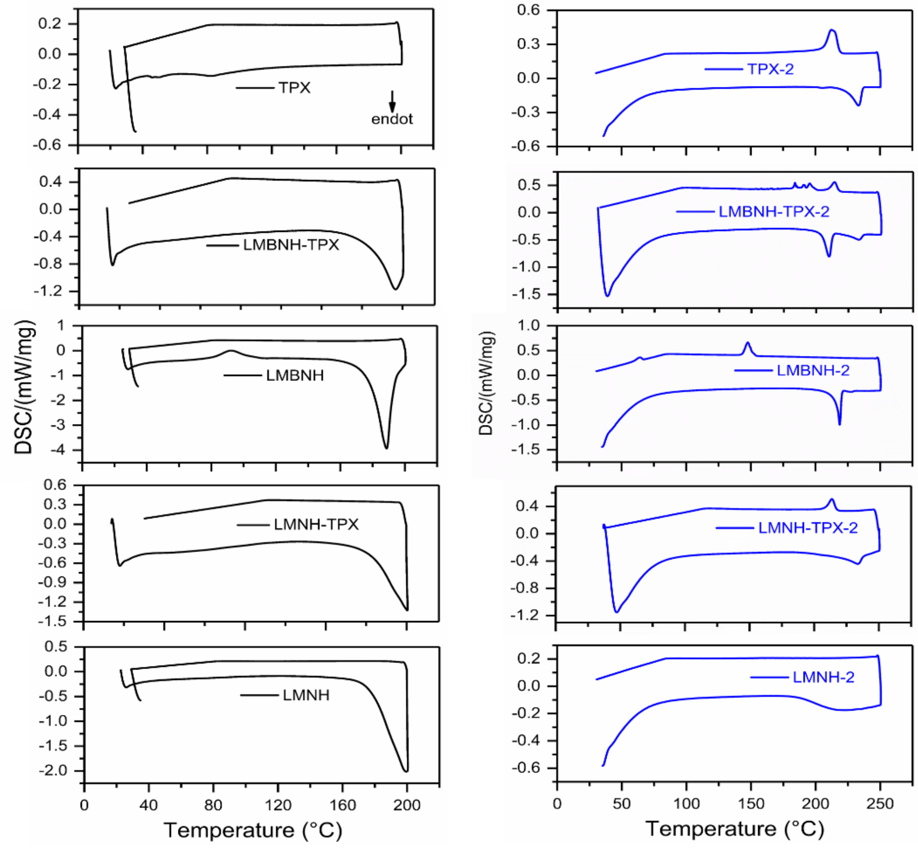

Figure S4. The first DSC thermal decompositions measurements of pure TPX, LMBNH-TPX, LMBNH, LMNH-TPX and LMNH (left), samples were heated from RT to 200 °C with a heating rate of 5 °C min^{-1} under 1 bar of H_2. The second DSC thermal decompositions measurements of pure TPX, LMBNH-TPX, LMBNH, LMNH-TPX and LMNH (right), samples were heated from RT to 250 °C with a heating rate of 5 °C min^{-1} under 1 bar of H_2.

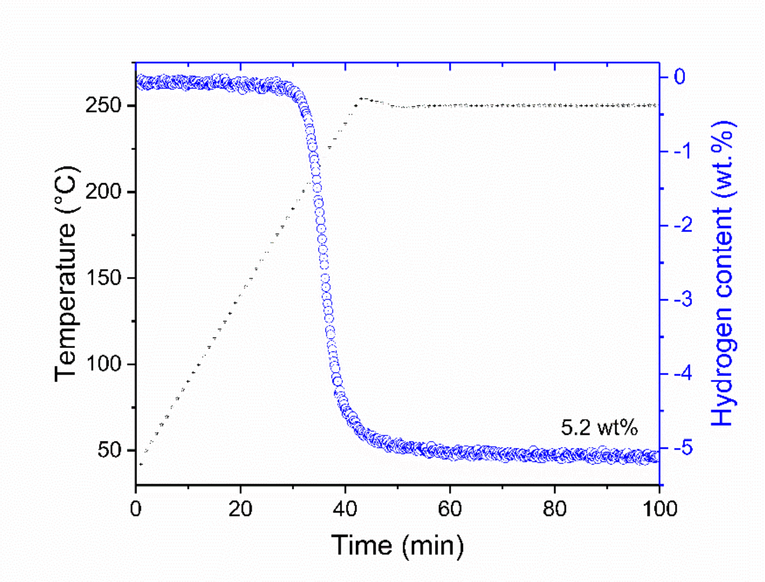

Figure S5. Temperature programmed dehydrogenation of the post-cycled LMNH-TPX, sample has been heated from RT to 250 °C with a heating rate of 5 °C min^{-1} under 1 bar of H_2.

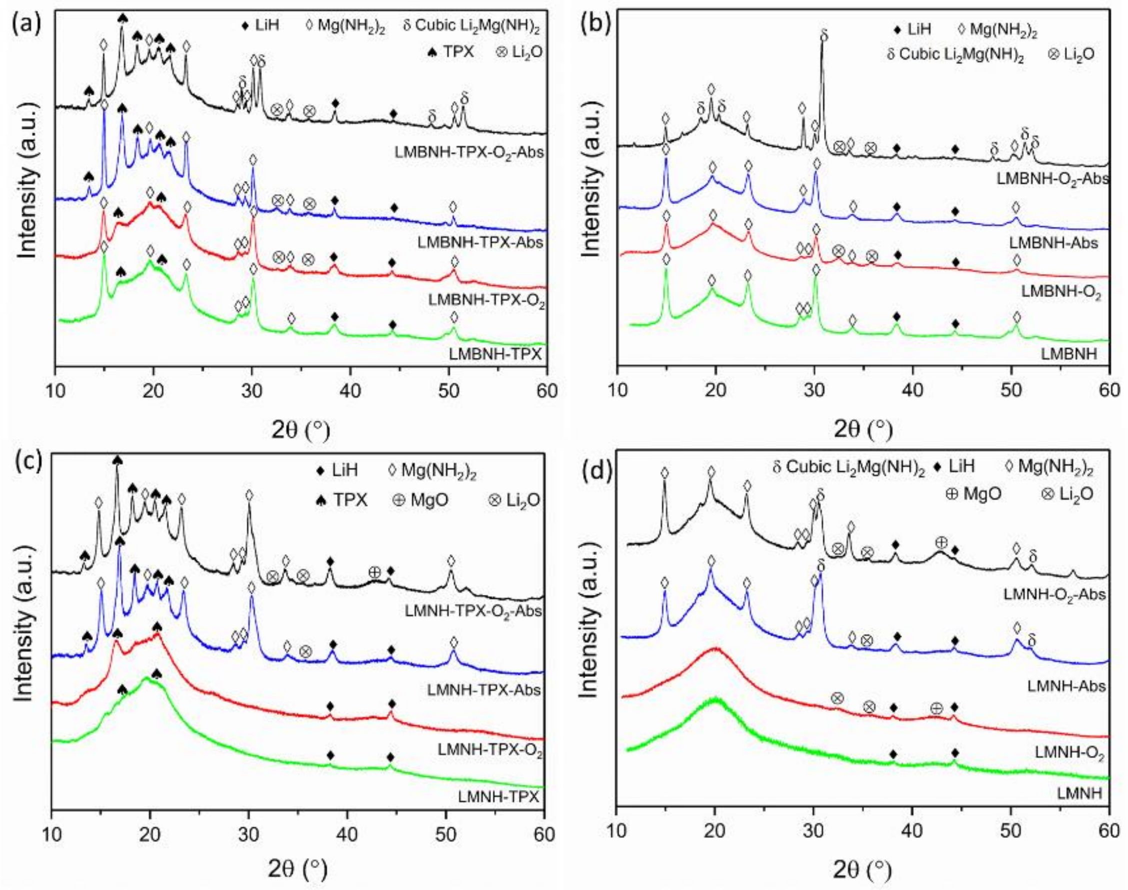

Figure S6. XRD patterns of LMBNH-TPX, LMBNH, LMNH-TPX, and LMNH after preparing, exposing to air 12h (O_2), and absorption (Abs).

Gas transport properties of TPX™

Table S1. Permeability (P), diffusion coefficient (D) and solubility coefficient (S) of freestanding thick film TPX™ membranes measured at 30 °C with the time-lag method.

	P [Barrer]*	D [10^{-10} m^2/s]	**S** [10^{-3} $cm^3_{STP}/(cm^3\ cmHg)$]
H_2	92.1	20.7	0.445
O_2	24.4	1.56	1.56
N_2	6.29	0.716	0.879
H_2O	177	0.0159	1112

* 1 Barrer = 10^{-10} [$cm^3_{STP}/(cm\ s\ cmHg)$]

Reference:

[S1] I. Blume, E. Smit, M. Wessling, C. Smolders, in: Macromolecular Symposia, Wiley Online Library, 1991, pp. 237-257.
[S2] H.L. Frisch, The Journal of Physical Chemistry, 61 (1957) 93-95

TOC

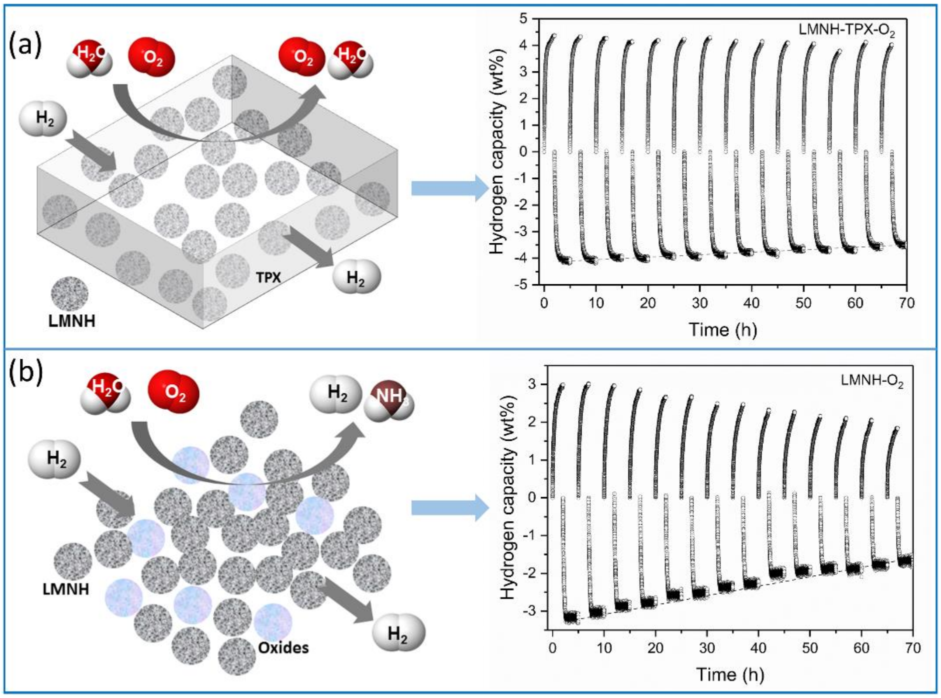

The amide-hydride systems remain stable in the polymeric matrix of polymethylpentene significantly improving the air stability of the metal hydrides. It shows a promising way to fabricate metal hydride-polymer composite energy storage materials that can be handled in ambient conditions.